Synergistic Experimental and Theoretical Studies of Luminescent−Magnetic Ln₂Zn₆ Clusters

Sayan Saha,[†] Krishna Sundar Das,[†] Tanu Sharma, Sukhen Bala, Amit Adhikary, Guo-Zhang Huang, Ming-Liang Tong, Arjit Ghosh, Benubrata Das, Gopalan Rajaraman,* and Raju Mondal*

Read Online

ACCESS | 📊 Metrics & More | 📖 Article Recommendations | 🆂🅸 Supporting Information

ABSTRACT: The present work is part of our ongoing quest for developing functional inorganic complexes using unorthodox pyridyl−pyrazolyl-based ligands. Accordingly, we report herein the synthesis, characterization, and luminescence and magnetic properties of four 3d−4f mixed-metal complexes with a general core of Ln_2Zn_6 (Ln = Dy, Gd, Tb, and Eu). In stark contrast to the popular wisdom of using a compartmental ligand with separate islands of *hard* and *soft* coordinating sites for selective coordination, we have vindicated our approach of using a ligand with overcrowded N-coordinating sites that show equal efficiency with both 4f and 3d metals toward multinuclear cage-cluster formation. The encouraging red and green photoluminescent features of noncytotoxic Eu_2Zn_6 and Tb_2Zn_6 complexes along with their existence in nanoscale dimension have been exploited with live-cell confocal microscopy imaging of human breast adenocarcinoma (MCF7) cells. The magnetic features of the Dy_2Zn_6 complex confirm the single-molecule-magnet behavior with befitting frequency- and temperature-dependent out-of-phase signals along with an U_{eff} value of ∼5 K and a relaxation time of 8.52×10^{-6} s. The Gd_2Zn_6 complex, on the other hand, shows cryogenic magnetic refrigeration with an entropy change of 11.25 J kg⁻¹ K⁻¹ at a magnetic field of 7 T and at 2 K. Another important aspect of this work reflects the excellent agreement between the experimental results and theoretical calculations. The theoretical studies carried out using the broken-symmetry density functional theory, *ORCA* suite of programs, and *MOLCAS* calculations using the complete-active-space self-consistent-field method show an excellent synergism with the experimentally measured magnetic and spectroscopic data.
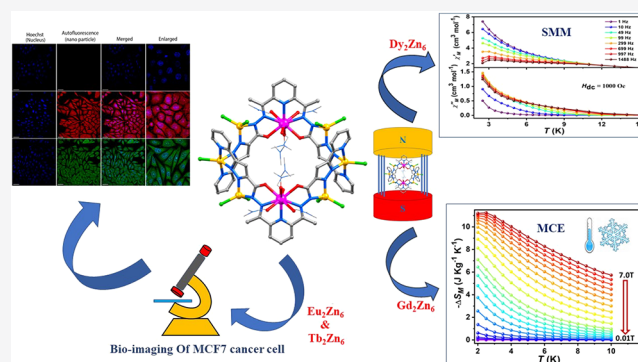
INTRODUCTION

Optimization of the desired physiochemical properties of value-added products using various nonconventional strategies remains the primary motive of researchers working on exploratory inorganic functional materials.[1−6] In a nutshell, unlike the purist inorganic chemists' approach of solving a mystery with orthodox methods, excelling materialistic properties of commercial importance are at the heart of these types of scientific endeavors.[7−9] Interestingly, most of the physiochemical features of inorganic compounds are strongly related to the electronic and magnetic interactions in terms of their valence orbital overlap of either among the metal centers or between the metal center and the functional moiety of coordinating organic ligands.[10−12] Naturally, any judicious plan aiming to boost the utility of the compound should put more emphasis on enhancing the interactions among the related functional orbitals.[13]

One such prime example would be 3d−4f mixed-metal complexes.[14−17] Notwithstanding the initial skepticism, the concomitant presence of transition metals and lanthanides for the construction of a polynuclear cage and clusters has proven

to be highly rewarding, with markedly improved magnetic, chemical, optical, and other physical properties.[18−23] Of particular interest is the deliberate mixing of f and d electrons to induce stronger interactions *vis-a-vis* individual d−d or f−f electrons to transcend the magnetic, electronic, and optical properties, and their mutual interplay is now well documented.[24,25] Subsequently, the last few decades have witnessed a phenomenal upsurge of interest in studies of mixed-metal complexes.[26,27] Almost every possible combination of 3d−4f complexes has been explored.[28−32] The emphasis of initial works is more or less "one-dimensional"; that is, they aim to optimize one particular property like magnetism or optics.[33−35] With advancement of the subject, however, other potential uses of these complexes soon become increasingly apparent.[36]
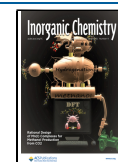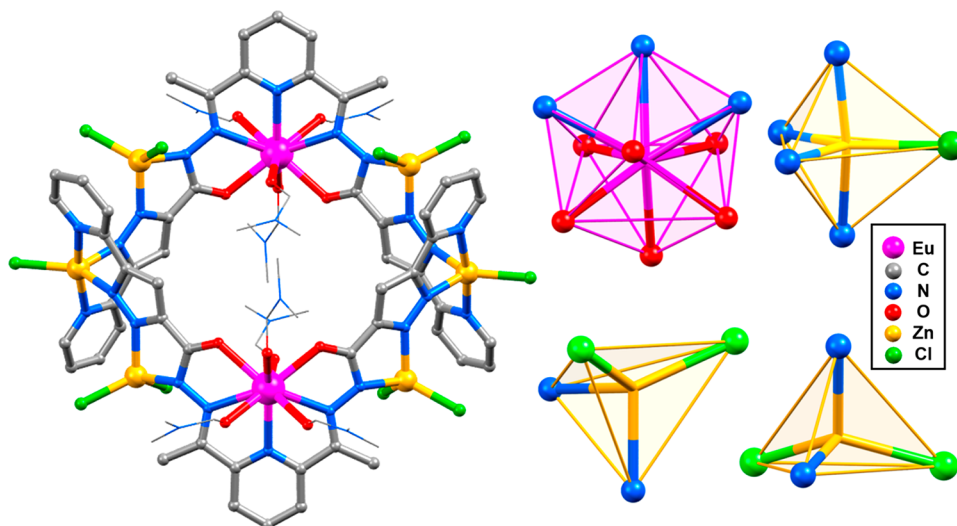
Figure 1. Perspective view of **Eu₂Zn₆**. The DMF molecules are shown in a wireframe model for clarity. Representations of a tricapped trigonal-prismatic geometry around the Ln atom and trigonal-bipyramidal and distorted tetrahedral geometries around the Zn atoms.

Moreover, instead of using randomly chosen pairs, a specific combination of 3d and 4f metals with the aim of culminating their characteristic properties starts to dominate the design strategy, aiming to *kill two birds with one stone*.[37] One such popular combination for a set of 3d–4f complexes would be magnetism and luminescence, which also coincides with the broad theme of this work.[38−40]

Single-molecule magnet (SMM) and magnetocaloric effect (MCE), *inter alia*, are the two most important lanthanide-magnetism topics that have tantalized the attention of both chemists and physicists in recent years.[41−44] The Dy^{3+} compounds, because of their significant anisotropy arising from large unquenched orbital angular momentum and a high energy reversal barrier, more-often-than-not show slow magnetic relaxation and dominate SMM studies.[45−48] On the other hand, the Gd^{3+} ion, by virtue of its large spin-only magnetic moment, weak superexchange interaction, and quenched orbital momentum, predominates the recent quest for low-cost, environmentally benign cryogenic technology using MCE-based magnetic refrigeration.[49−53] Notwithstanding their individual magnetic features, the combination of Dy^{3+} and Gd^{3+} with transition metals is often found to excel the magnetic behavior.[54−57]

The precise and fixed color-sensitized luminescence of Tb^{3+} and Eu^{3+} has enabled the use of the corresponding compounds as probes for optical sensing and imaging.[58−61] This is precisely where the concept of 3d–4f complemetarity can come in really handy. Recent reports show the using combinations of Tb^{3+} and Eu^{3+} alongside IIB metals with d^{10} conformations, such as Zn^{2+} or Cd^{2+} with their complementary photoluminescence (PL) characteristics, is an excellent strategy for generating improved luminescent materials.[62−67] Resultant 3d–4f complexes with improved luminescence behavior offer a wide range probes for a number of biomedical applications.[68] This is further complemented with the nanoscopic dimension of discrete inorganic complexes that can easily internalize into the cell and thereby fulfill the primary prerequisite of cellular studies including imaging and sensing.[69]

Recent advancement in theoretical studies, both individually as well as combined with experimental results, also played a pivotal role in understanding the all-important magnetic exchange parameters and their underlying relationship with the structural parameters.[70] This is particularly true for polynuclear clusters, where the final magnetic features are often acutely entangled with multiple exchange constants.[71] It is almost next to impossible to extract the exchange coupling exclusively from the magnetic data, but the computational tools come in handy.[72]

In this paper, we report four luminescent–magnetic 3d–4f mixed-metal complexes with a general formula of $[Ln^{III}_2Zn^{II}_6(CPPC)_2(DMF)_8Cl_{10}](DMF)_2$ (**Ln₂Zn₆**; Ln = Dy, Gd, Tb, and Eu; DMF = dimethylformamide), which were synthesized with a new semirigid, heavily N-rich multidentate ligand, (10*E*)-*N'*-[1-[6-[[(*E*)-1-[5-(pyridin-2-yl)-1*H*-pyrazole-3-carboylimino]ethyl]pyridin-2-yl]ethylidene]-3-(pyridin-2-yl)-1*H*-pyrazole-5-carbohydrazide (H₂CPPC). The intriguing luminescent features of Eu- and Tb-based mixed-metal complexes, coupled with their nanodimensonal existence in solution as well as nontoxic nature, make them strong candidates for cellular studies. As such, they have been successfully exploited for cellular imaging of human breast adenocarcinoma (MCF7) cells. On the other hand, the magnetic properties of the Dy and Gd complexes have been investigated in detail. Furthermore, complete-active-space self-consistent-field (CASSCF) theoretical calculations on the mixed-metal complexes using *MOLCAS* software show excellent synergy with the experimental results.

■ RESULTS AND DISCUSSION

Ligand Design. In a nutshell, the judicious ligand design principle for 3d–4f compounds demands a tricky fusion of two contrasting yet compatible functional moieties within a single chassis, which can sustain the disparate coordination behaviors of lanthanides and transition metals. The most commonly used ligands for these purposes are compartmental in nature featuring two juxtaposed pockets, individually fitted with hard O-donor and soft N-donor sites, respectively, for 4f and 3d metals (Figure S1). In stark contrast to this popular wisdom, our pyridine–pyrazole-based N-rich ligands show equal efficiency with both 4f and 3d multinuclear cage-cluster formation and therefore bucks the trend of using separate islands of hard and soft coordinating sites for selective
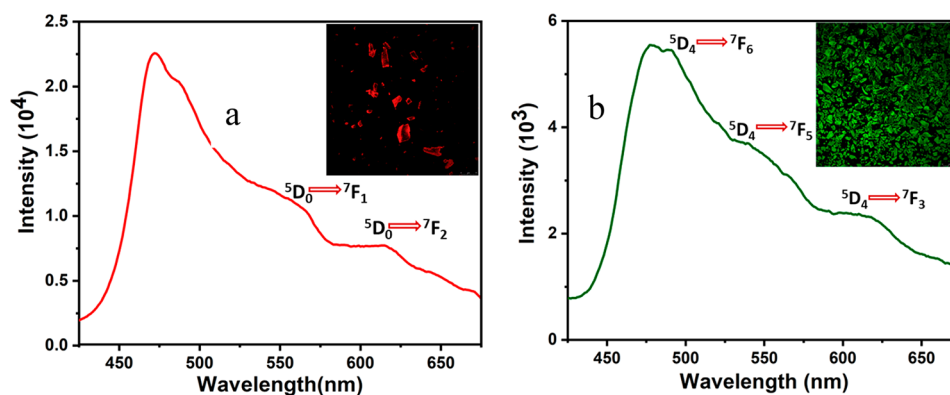
Figure 2. (a) PL spectra of **Eu$_2$Zn$_6$**. Inset: Crystals emitting a red luminescence color under a UV lamp. (b) PL spectra of **Tb$_2$Zn$_6$**. Inset: Crystals emitting a green luminescence color under a UV lamp.

coordination. However, the main point of contention remains the challenge of attaining the *sine qua non* high coordination number of Ln by accommodating the highest number of coordinating sites while ensuring the lowest detrimental steric hindrance of noncoordinating organic moieties. Our approach is to outweigh detrimental steric crowding with the overcrowding of coordinating sites. We took our inspiration from the ironic multidentate lining feature of a Venus flytrap and prepared our titular ligand, H$_4$CPPC (Figure S1), analogously studded with as many as 13 coordinating sites in a half-moon style.

Structural Description. The current complexes of **Ln$_2$Zn$_6$** (Ln = Dy, Gd, Tb, and Eu) were synthesized in excellent crystalline form under similar refluxing conditions using LnCl$_3$· 6H$_2$O (Ln = Dy, Gd, Tb, and Eu), anhydrous ZnCl$_2$, and H$_2$CPPC at 80 °C. All of the complexes were also routinely characterized by Fourier transform infrared (FT-IR) spectroscopy, elemental analysis, mass spectroscopy, and single-crystal X-ray diffraction analyses. The **Ln$_2$Zn$_6$** compounds are isostructural in nature; thus, the structural aspects of only **Eu$_2$Zn$_6$** will be discussed here. The structural details, coordination geometries, crystallographic table, selected bond lengths and angles, and additional perspective views of all of the compounds are reported in the Supporting Information.

Single-crystal X-ray diffraction reveals that the **Eu$_2$Zn$_6$** complex crystallizes in the triclinic $P\bar{1}$ space group and consists of a neutral discrete [Eu$^{III}_2$Zn$^{II}_6$(CPPC)$_2$(DMF)$_8$Cl$_{10}$](DMF)$_2$ entity (Figure 1). The asymmetric unit comprises of 2 Eu^{III} centers, 6 Zn^{II} centers, 2 deprotonated anionic ligand moieties, 8 coordinated DMF molecules, 10 coordinated chloride anions, and 2 lattice DMF molecules. As expected, H$_2$CPPC adopts a two-prong pendent orientation, where the central pyridine moiety acts as the pendent and the terminal pyridine−pyrazole moiety constitutes each prong. Topologically, a bangle-shaped close loop is formed when four exo-oriented pyridine−pyrazole moieties of two ligand molecules coordinate to two Zn atoms, while the remaining sites of the trigonal-bipyramidal geometry of pentacoordinated metal centers are occupied by Cl ions. As a result, the pyrazolate N and amide N atoms reside on the outer periphery of the loop and coordinate to two tetrahedral Zn centers, whose remaining two sites are occupied by terminal Cl ions. The values of the Zn−N bond lengths cover the ranges from 2.017(4) to 2.099(4) Å, while the Zn−Cl bond lengths lie within the range of 2.2177(14)−2.2708(16) Å. On the other hand, two Eu atoms get buried deep inside the

trough region of the ligand and linked to the central pyridine moiety, with a Eu···Eu separation of 10.391 Å. The nonacoordinated Eu ions can best be described as a tricapped trigonal-prismatic geometry with a N$_3$O$_6$ coordination environment. The coordination is associated with one pyridyl N, two emine N, and two enolate O atoms, while the remaining four coordination sites are fulfilled by four DMF molecules. The Eu−O bond lengths are in the range of 2.351(3)−2.459(3) Å, while the Eu−N bond lengths are in the range of 2.553(4)− 3.247(5) Å. From a topological point of view, the six coplanar Zn atoms can be envisaged as the vertices of an elongated hexagon, while two Ln atoms reside on either side of the plane with an out-of-plane displacement value of 2.45 Å (Figure S20). The high coordination number adopted by the lanthanides prompts us calculate the continuous shape measure[73] values by Shape analysis, which confirms that the lanthanides adopt a geometry that closely resembles a muffin. The details of calculation and results are tabulated in Table S1.

PL Properties and Bioimaging Applications. Individually, both lanthanide compounds and d^{10} metal complexes are well-known luminescent materials, especially the lanthanides for their unique optical features. As per the theme of this paper, we were therefore naturally interested to see the combined effect on mixed-metal complexes, and accordingly a thorough investigation was carried out. The solid-state UV−vis spectra recorded with thin films of the **Eu$_2$Zn$_6$** and **Tb$_2$Zn$_6$** complexes show the absorption maxima at 304 and 340 nm, respectively (Figure S2). A little hump found around 403 nm for **Eu$_2$Zn$_6$** and 410 nm for **Tb$_2$Zn$_6$** can be attributed to the corresponding charge-transfer phenomena between the ligand to metal centers. We have also cross-checked the results with theoretical values for each complex. CASSCF calculations have been performed using the *ORCA* suite of programs in order to evaluate the absorption spectra of the **Eu$_2$Zn$_6$** and **Tb$_2$Cl$_6$** complexes (Figure S3). The λ_{max} value from this computation was around 351.1 nm for the Eu complex, whereas for the Tb complex, it is 329.8 nm, which significantly matches what we have observed in the experimental plots. These values are in agreement with the experimental λ_{max} values of ∼350 and ∼300 nm for the Eu and Tb complexes, respectively. These bands can be attributed to the $^7F \rightarrow {}^5D$ transitions in both of these complexes. Further, from the spin-orbit *RASSI* set of calculations, we estimated the difference between the heptet and quintet states, and it was found to be around 313 and 289 nm for the **Eu$_2$Zn$_6$** and **Tb$_2$Zn$_6$** complexes, respectively, which again reflects the difference between the Eu and Tb spectra,
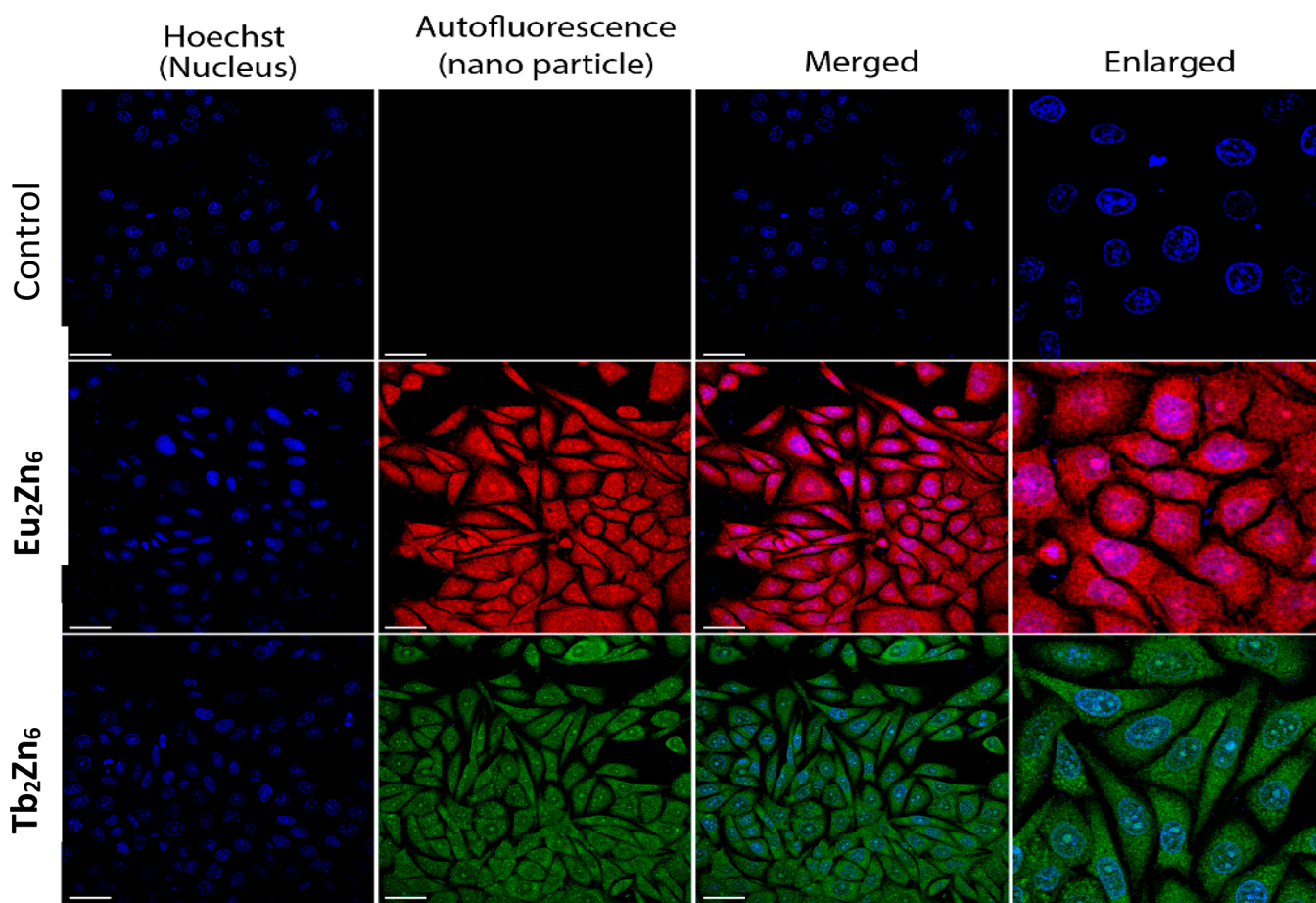
Figure 3. Representative live-cell confocal microscopic images showing localization of Eu_2Zn_6 (10 μM, red) and Tb_2Zn_6 (10 μM, green) in the nucleus and cytoplasm of MCF7 cells, as monitored by intrinsic fluorescence of the drugs (Eu_2Zn_6 red channel, middle panel, and Tb_2Zn_6 green channel, middle panel) and with Hoechst 33342 (blue channel, left panel) used as a nuclear marker. The right panel shows the merged images.

and if rescaled by $\sim$3000$-$1000 cm^{-1}, it also comes in the same order as that of the experimental results. These differences may be attributed to the fragmentation approach of the calculations.

Furthermore, the solid-state PL data collected with the thin-film form over a quartz surface yield the characteristic peak at 614 nm for the Eu_2Zn_6 complex, which corresponds to the $^5D_0 \rightarrow {}^7F_2$ transition (Figure 2). The PL data of the Tb_2Zn_6 complex, on the other hand, show the peaks at 556 and 625 nm due to the $^5D_4 \rightarrow {}^7F_5$ and $^5D_4 \rightarrow {}^7F_3$ transitions, respectively. As a result, the complexes are deemed to be very much suitable as a fluorescence probe for bioapplications like cellular imaging.

Bioinvestigations on the cells, however, demand the fulfillment of some preconditions. First and foremost, the stability of the compound in the probe medium needs to be established to ascertain that the material used for the investigation is indeed the complex and remains intact throughout the study. The combined electrospray ionization mass spectrometry (ESI-MS) spectra in dimethyl sulfoxide (DMSO) and matrix-assisted laser desorption/ionization (MALDI) spectra in a dihydroxybenzoic acid matrix confirm the existence of both complexes in the solution state. The ESI-MS spectrum of Tb_2ZN_6 shows a peak at m/z 1176, while the spectrum of Eu_2Zn_6 shows peaks of fragmented mass of the complex. The MALDI spectra show multiple peaks at m/z 920, 1182, and 1348 for Eu_2Zn_6, and the peaks at m/z 1357, 1420,

and 1456 for Tb_2Zn_6 correspond to fragmentation of the complexes (Figure S4).

Another important aspect is the solution-phase dimension of the complexes, whose internalization into the cell is the primary determinant of successful cellular experiments. The dynamic light scattering (DLS) experiments show that the particle size of Tb_2Zn_6 is around 100 nm, while that of Eu_2Zn_6 is in the range of 100$-$1000 nm (Figure S5), which fall well within the critical dimension of cell permeability. Further corroborating evidence comes from the transmission electron microscopy (TEM) images, which show the aggregation of numerous particles of an approximate dimension of 100 nm (Figure S6). Furthermore, the selected-area electron diffraction data from TEM confirms the crystalline nature of the nanoparticles (Figure S7). Energy-dispersive X-ray spectroscopy analysis performed on the nanoparticles was found to contain both Ln and Zn metals along with C, N, O, and Cl (Figure S8) and hence unequivocally confirms the existence of complexes as stable, crystalline, nanoscale-sized, photoluminescent materials suitable for biomedical applications.

The Eu_2Zn_6 and Tb_2Zn_6 complexes capable of producing characteristic red and green fluorescence were utilized for the cellular imaging of MCF7 cells using live-cell confocal microscopy, while Hoechst 33342 (Blue) was used as the marker of the cell nuclei. The routine cell survival MTT assay experiments of incubating complexes with MCF7 cells did not manifest any significant adverse effect, indicating the nontoxic
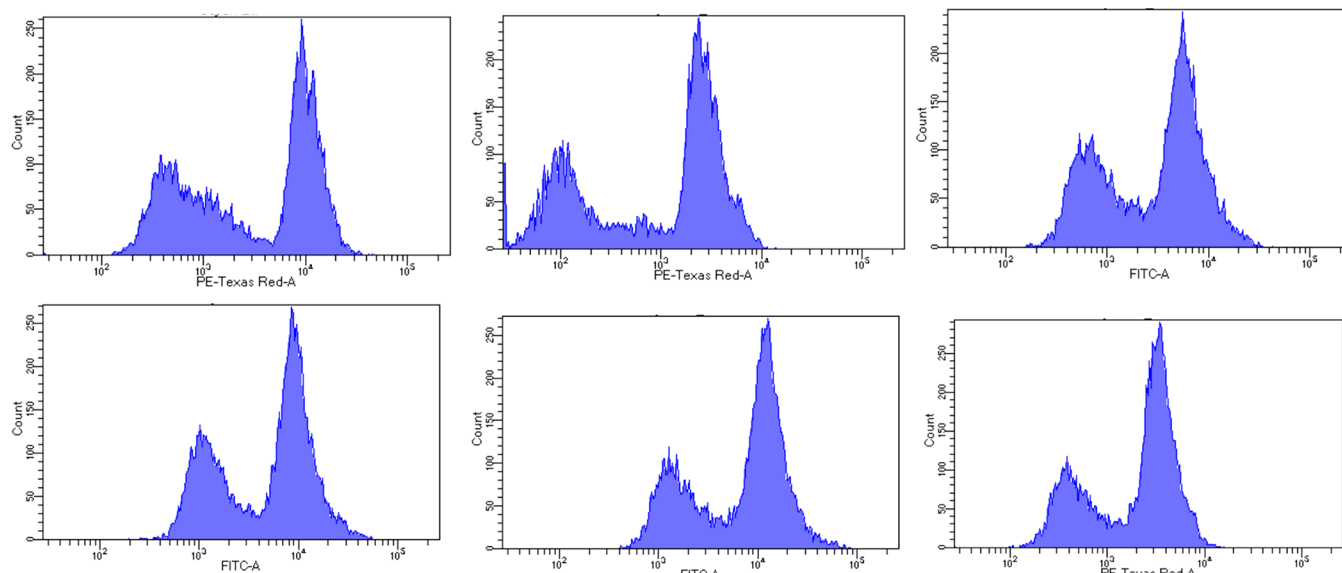
Figure 4. First row: Intensity versus count plot of $\mathbf{Eu_2Zn_6}$ in the initial stage of time (t) = 0, 6, and 12 h. Second row: Intensity versus count plot of $\mathbf{Eu_2Zn_6}$ in the initial stage of t = 0, 6, and 12 h.

nature of the compound (Figure S9). The nanoscopic sizes of the compounds are consistent with the DLS and microscopic data and did permeate through the membranes of the MCF7 cells after 6 h of incubation. Rapid cellular uptakes of both compounds were observed after their incubation with the cells, but the nuclei revealed no significant deformation. The enlarged live-cell confocal images unequivocally confirm the accumulation of the fluorescent probes in both the nucleus and cytoplasm (Figure 3). Furthermore, distinct fluorescence colors, red for $\mathbf{Eu_2Zn_6}$ and green for $\mathbf{Tb_2Zn_6}$, provide extra advantages in terms of color-coded cellular imaging. The compatibility of complexes as fluorophores was further validated with fluorescence-activated cell sorting studies using 546 and 488 nm lasers respectively for red fluorescence (Texas-Red) and green fluorescence (FITC), while the corresponding emissions were recorded at 613 and 519 nm. The study clearly supports the usefulness of the complexes as a steady source of fluorescence, which is again related to their stability within the cell environment. Further corroboration comes from the forward- and side-scatter plots showing a negligible reduction in the fluorescent intensity/count even after 12 h time intervals (Figures 4 and S10).

Magnetic Study. The above improved PL properties obtained fully justify the notion of mixing 3d−4f orbitals to transcend the optoelectronic properties. Naturally, the obvious question then arose as to whether a similar trend could also be replicated for the magnetic properties. In order to answer that, detailed experimental as well as theoretical magnetic investigations were carried out. The direct-current (dc) magnetic susceptibility data collected on a polycrystalline sample of the $\mathbf{Gd_2Zn_6}$ complex are shown in the form of a $\chi_M T$ (χ_M = molar magnetic susceptibility) versus T plot (Figure 5). At 300 K, the $\chi_M T$ value of the Gd_2Zn_6 complex is 15.75 cm^3 mol^{-1} K, which is close to the theoretical value of 15.62 cm^3 mol^{-1} K ($^8S_{7/2}$ and $g = 2$) for two Gd^{3+} ions. With a decrease in the temperature, $\chi_M T$ remains almost constant down to ~12 K, and below that temperature, the $\chi_M T$ plot decreases and a minimum $\chi_M T$ value of 15.35 cm^3 mol^{-1} K is obtained at 2 K.

For further investigations, a $\chi_M T$ versus T plot was fitted using the binuclear model (Figure 6b), and the fitting yields J =
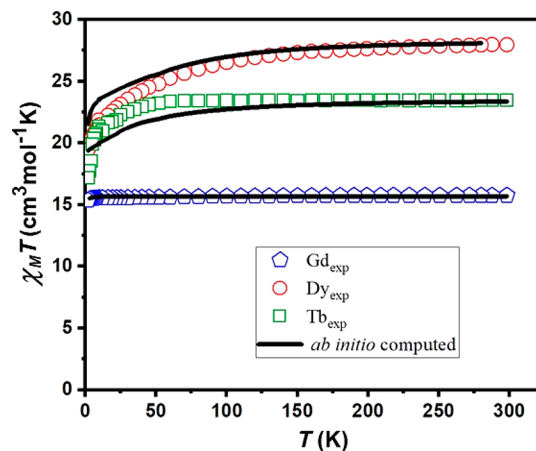
Figure 5. Temperature-dependent $\chi_M T$ versus T plot for $\mathbf{Ln_2Zn_6}$ (Ln = Gd^{3+}, Dy^{3+}, and Tb^{3+}) complexes.

−0.0003 cm^{-1} and g = 2.0. A very low and positive J value suggests very weak antiferromagnetic interactions between two Gd^{3+} centers, as one would expect for a dinuclear unit separated by 10.39(6) Å, and magnetic exchange passes through diamagnetic Zn^{2+} ions (Figure 6a). There is one exchange pathway in the $\mathbf{Gd_2Zn_6}$ complex that is the interaction between two Gd1 and Gd2 ions, termed as J. To evaluate the exchange coupling constant J, the following Hamiltonian has been used:

$$\hat{H} = -2J\{(\hat{S}_{Gd1} \cdot \hat{S}_{Gd2})\}$$

Broken-Symmetry Density Functional Theory (BS-DFT) Calculations. The magnetic exchange coupling J is estimated to be +0.003 cm^{-1} in the $\mathbf{Gd_2Zn_6}$ complex. The computed Mulliken spin density is found to be +7.029 on both Gd^{III} in high spin (HS) and +7.029 on Gd1 and −7.029 on Gd2 in BS, respectively, indicative spin polarization being in operation, as seen in earlier {Gd$_2$} systems.[74] (Figure S11). Two Gd^{III} ions are 10.39 Å apart from each other; although there is a possible superexchange pathway, there are three Zn^{II} ions between them, and hence this is expected to be very weak,
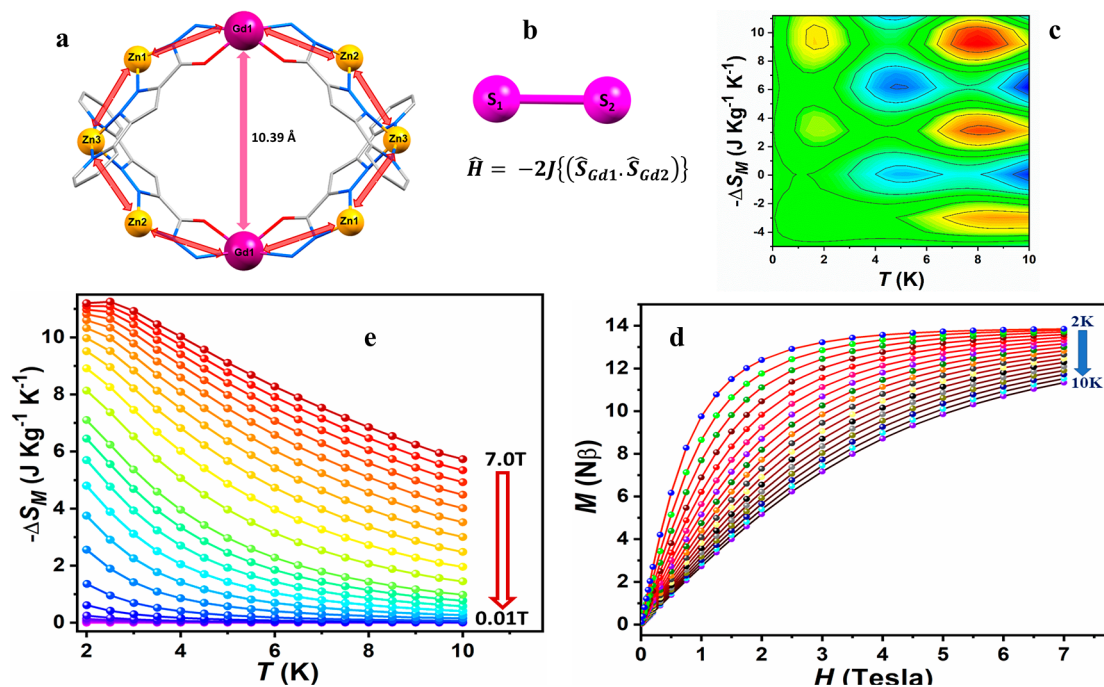
Figure 6. (a) Schematic diagram of the interaction between two Ln atoms. (b) Corresponding Hamiltonian to calculate J. (c) Contour plot of magnetic entropy change $(-\Delta S_M)$. (d) Field-dependent isothermal magnetization and (e) temperature dependencies (2−10 K) of $-\Delta S_M$ for **Gd₂Zn₆** as obtained from the magnetization data.
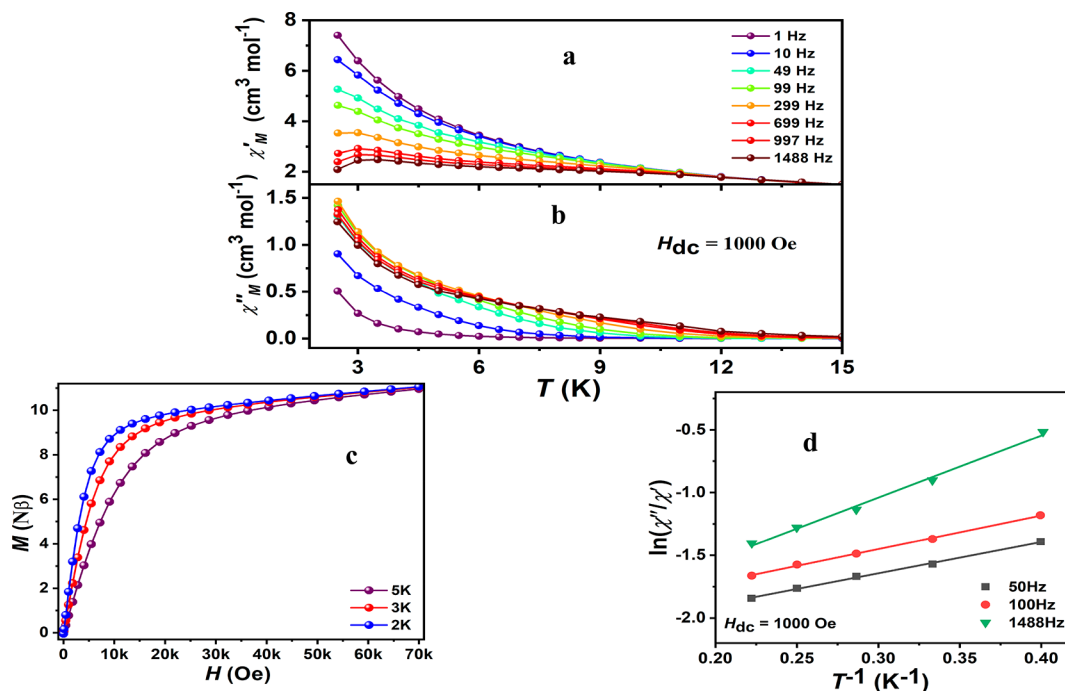
Figure 7. Temperature dependence of the (a) in-phase (χ') and (b) out-of-phase (χ'') ac magnetic susceptibility for **Dy₂Zn₆** in the temperature range of 2−15 K and at a dc field of 1000 Oe. (c) Frequency dependence of the in-phase (χ') field-dependent isothermal magnetization of **Dy₂Zn₆**. (d) Plot of $\ln(\chi''/\chi')$ versus $1/T$.

as estimated. The extracted J parameter for the Gd−Gd pair in complex **Gd₂Zn₆** was rescaled to the spin of the Dy^{III} ($S = {}^5/_2$) ions by multiplying them by the spin of the corresponding metal ion and divided by the spin of Gd^{III} ($S = {}^7/_2$). The rescaled J parameters for the **Tb₂Zn₆** and **Dy₂Zn₆** complexes were found to be −0.00025 and −0.0002 cm^{-1}, respectively.

	Gd1	Gd2	S
HS	↑	↑	7
BS	↑	↓	0
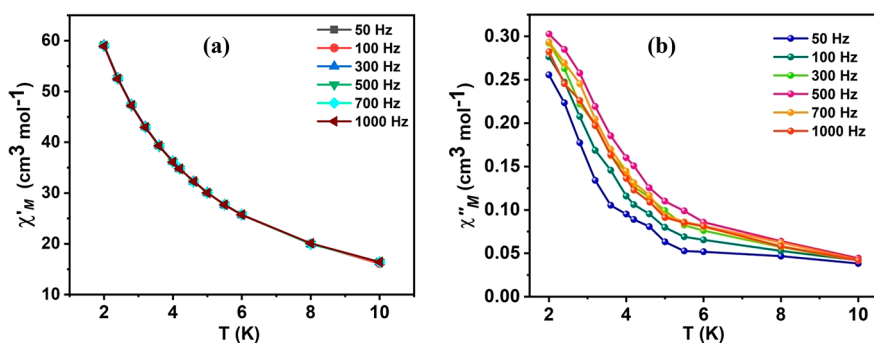
Figure 8. Temperature dependence of (a) in-phase (χ') and (b) out-of-phase (χ'') ac magnetic susceptibility for **Tb₂Zn₆** in the temperature range of 2−10 K and at the dc field of 1000 Oe.

Table 1. Energies (cm⁻¹) of the Lowest Doublets and g Tensors of the Individual Lanthanide Magnetic Centres Associated with Each State for Complexes Tb₂Zn₆ and Dy₂Zn₆[a]

	Tb1				Tb2			
state	E (cm⁻¹)	g_x, g_y, g_z	tunnel splitting	θ	E (cm⁻¹)	g_x, g_y, g_z	tunnel splitting	θ
1	0.0/0.3	17.573	0.3		0.0/0.3	17.556	0.3	
2	83.5/86.5	14.127	3	2.8	83.2/86.3	14.108	3.1	2.8
3	172.1/193.9	10.240	21.8	5.2	172.2/193.89	10.215	21.7	5.2
4	227.5/266.7	5.294	39.2	170.9	227.4/266.6	5.279	39.2	170.9
5	271.6/302.0	4.129	30.4	49.4	271.5/302.0	4.126	30.5	49.2
6	308.1/345.5	1.062	37.4	62.4	308.1/345.5	1.054	37.4	62.7

	Dy1					Dy2			
KD	E (cm⁻¹)	g_x	g_y	g_z	θ	E (cm⁻¹)	g_x	g_y	g_z	θ
1	0.0	0.026	0.056	19.345		0.0	0.026	0.056	19.373	
2	108.8	0.658	1.886	17.104	46	108.8	0.659	1.890	17.125	46
3	144.0	0.523	1.672	15.471	53.5	144.0	0.525	1.673	15.486	53.5
4	182.3	0.331	1.764	14.773	2.8	182.3	0.331	1.763	14.809	2.8
5	236.7	0.321	1.603	12.422	18.3	236.7	0.321	1.604	12.432	18.3
6	264.4	7.674	5.963	2.672	85.2	264.4	7.669	5.961	2.674	85.2
7	298.9	1.582	3.939	12.989	87.0	298.9	1.579	3.941	12.993	87.0
8	465.6	0.001	0.015	19.333	93.5	465.6	0.001	0.015	19.355	93.5

[a]The angle between the ground-state g_{zz} and respective excited-state g_{zz} axes is represented by θ.

The corresponding M (Nβ) versus H was plotted in the temperature range of 2−10 K and in the magnetic field of 0−7 T (Figure 6d). The magnetization value increases with a rise in the magnetic field as well as with a decrease in the temperature. At a temperature of 2 K, the isotherm is almost flattened from ∼5 T and, hence, shows the sign of saturation. The maximum magnetization value of 13.89 Nβ was obtained at 2 K and 7 T. It is close to the theoretical value of 14 Nβ. Therefore, the compound is isotropic in nature. Subsequently, the magnetic entropy change was calculated using the magnetization data to examine whether **Gd₂Zn₆** shows any MCE.

The magnetic entropy change was calculated using the isothermal magnetization data shown in Figure 6d and the following Maxwell relationship:

$$\Delta S(T, \Delta H) = \int [\delta M(T, H)/\delta T]_H \, dH$$

The results are characterized as a |−ΔS_M| versus T plot (Figure 6e). With increasing magnetic field, the −ΔS_M value increases, and the highest value was obtained at a temperature of 2 K. The maximum entropy change of 11.25 J kg⁻¹ K⁻¹ was obtained at 2 K and a magnetic field of 7 T. The reported |−ΔS_M| value is relatively low because of the large diamagnetic contribution of Zn²⁺ ions.

The dc magnetic susceptibility of **Dy₂Zn₆** and **Tb₂Zn₆** is also investigated at variable temperature because of their phase purity after powder X-ray diffraction analysis (Figure S12). The room temperature $\chi_M T$ values of **Dy₂Zn₆** and **Tb₂Zn₆** are 27.97 and 23.47 cm³ mol⁻¹ K, respectively, which closely match the theoretical values of 28.34 and 23.64 cm³ mol⁻¹ K for two nonmagnetically interacting Dy³⁺ ions (⁶H₁₅/₂, $S = ^5/_2$, and $g = ^4/_3$) and Tb³⁺ ions (⁷F₆ and $g = ^3/_2$). Upon decreasing temperature, the $\chi_M T$ value of **Dy₂Zn₆** decreases slightly up to 100 K and reaches a value of 26.53 cm³ mol⁻¹ K, but below 100 K, the value decreases sharply, and at 2 K, the value reaches 19.48 cm³ mol⁻¹ K. The decrease of the $\chi_M T$ value of **Dy₂Zn₆** can be attributed to thermal depopulation of the Stark sublevels.

However, for **Tb₂Zn₆**, the $\chi_M T$ value remains constant down to 60 K, reaches a value of 23.40 cm³ mol⁻¹ K, and decreases sharply until 2 K with a value of 15.86 cm³ mol⁻¹ K. Like the Dy analogue, the decrease of the $\chi_M T$ value at lower temperature can also be rationalized from thermal depopulation of the Stark sublevels.

The extracted J parameter for the Gd−Gd pair in complex **Gd₂Zn₆** was rescaled to the spin of the Dy³⁺ ($S = ^5/_2$) ions by multiplying them by the spin of the corresponding metal ion and divided by the spin of Gd³⁺ ($S = ^7/_2$). In this way, the
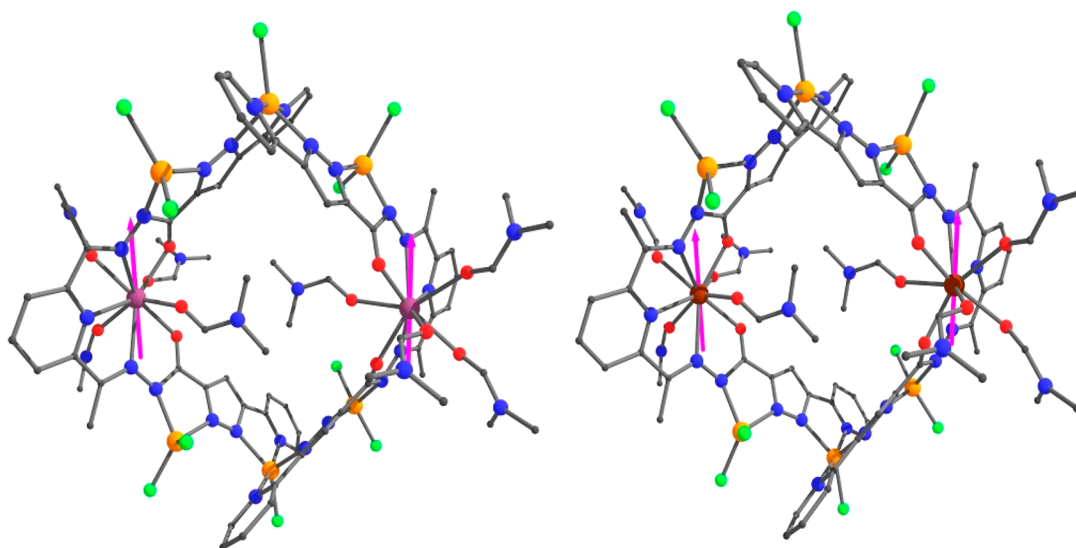
Figure 9. g_{zz} orientation on the Ln^{III} ions in the **Tb$_2$Zn$_6$** and **Dy$_2$Zn$_6$** complexes, where Tb is violet, Dy is maroon, C is dark gray, O is red, N is blue, Zn is dark yellow, and Cl is green. H atoms are omitted for clarity.

Table 2. Energy (cm^{-1}) for the Low-Lying Exchange Doublets Obtained from *POLY_ANISO* Simulation for Dy$_2$Zn$_6$ and Tb$_2$Zn$_6$

Tb$_2$Zn$_6$			Dy$_2$Zn$_6$		
energy/cm^{-1}	tunnel splitting	g_{zz}	energy/cm^{-1}	tunnel splitting	g_{zz}
0.000/0.338	0.338	24.966	0.000/0.000	3×10^{-6}	0.029
0.347/0.686	0.339	1.174	0.236/0.236	2×10^{-6}	38.717
83.211/83.254	0.043	0.001	108.848/108.848	2×10^{-4}	0.036
83.553/83.598	0.045	0.001	108.857/108.857	3×10^{-4}	33.600
86.308/86.346	0.038	0.001	108.989/108.989	2×10^{-4}	0.028
86.651/86.689	0.038	0.001	109.005/109.006	6×10^{-5}	33.556
166.465/169.556	3.091	18.263	217.639/217.642	3×10^{-3}	0.023
169.564/172.655	3.091	8.107	217.823/217.825	2×10^{-3}	34.230

rescaled *J* parameters for **Tb$_2$Zn$_6$** and **Dy$_2$Zn$_6$** were found to be −0.00025 and −0.0002 cm^{-1}.

The field dependence of magnetization *M* versus *H* plot does not meet the saturation level when a maximum external field of 7 T is applied for complex **Dy$_2$Zn$_6$**. The magnetization value is 11.05 Nβ at 7 T (Figure 7c) for two Dy^{3+} ions, which is much lower than the expected value of 20 Nβ for two Dy^{3+} ions.

In order to investigate dynamic magnetic behavior, the variable-temperature alternating-current (ac) susceptibility measurements were performed on complex **Dy$_2$Zn$_6$** at 0 and 1000 Oe dc field in the temperature range of 2−15 K (Figure 7a,b). However, there was no maximum of the χ'' signals under 0 Oe dc field because of the very fast quantum tunnelling of magnetization (QTM) through the spin/reversal barrier. To suppress this QTM partially/fully, the ac magnetic susceptibility was obtained under a dc field of 1000 Oe. Hence, the QTM is partially suppressed, and distinct signals are obtained. Therefore, the complex shows slow magnetic relaxation, which supports the SMM behavior. So, we cannot calculate the energy barrier (U_{eff}) and relaxation time (τ_0) through the conventional Arrhenius model (Figure 7d). Considering only one relaxation process, we calculate the rough energy barrier (U_{eff}) and relaxation time (τ_0) using the Debye model with the help of the following equation:

$$\ln(\chi''/\chi') = \ln(2\pi\nu\tau_0) + E_a/k_B T$$

The best-fitting data gave us an estimated U_{eff} of ∼5 K and τ_0 of 8.52×10^{-6} s, and this τ_0 value falls in the normal range of SMMs ($10^{-5}−10^{-11}$ s).[75] We also collected the ac magnetic data for **Tb$_2$Zn$_6$**, but proper signals are lacking in the zero field. However, at the applied field of 0.1 T, **Tb$_2$Zn$_6$** shows temperature-dependent out-of-phase susceptibility, indicating SMM behavior (Figure 8). Although no maxima were observed, henceforth the activation energy was not calculated.

Theory of Magnetic Relaxation. We have performed *ab initio* calculations on the X-ray structures of **Dy$_2$Zn$_6$** and **Tb$_2$Zn$_6$** complexes to understand the electronic structure and orientation of spin projections on each Ln^{III} center using *MOLCAS 8.2*. The six energy states in the **Tb$_2$Zn$_6$** complex are separated by 0−345.5 cm^{-1} (Table 1), whereas as expected in the **Dy$_2$Zn$_6$** complex, this separation is more, and in these complexes, these states are separated by 0−465.5 cm^{-1} (Table 1). The main magnetization axis on the Ln^{III} ion is found to be oriented between the imine N and amide O. The g_{zz} axes on both Ln^{III} ions are parallel to each other (Figure 9). The value of ground-state g_{zz} of both Tb1 and Tb2 is ≈17.5, and similarly the **g** tensor ($g_x = 0.026$, $g_y = 0.056$, and $g_z \approx 19.345$) for the Dy1 and Dy2 ions in the **Dy$_2$Zn$_6$** complex also shows almost negligible ground-state transverse anisotropy, indicating axial behavior for the ground-state KD, but the magnetic moment of the first excited state was found to be tilted by 46°, which points toward very high QTM. However, in both Tb1 and Tb2

of the Tb_2Zn_6 complex, a large tunnel splitting of around 0.3 cm^{-1} was found.

In order to justify the experimentally observed relaxation dynamics and to extract the Gd−Gd exchange interaction, we performed simulation of the experimental magnetic susceptibility data using the *POLY_ANISO* program implemented in the *MOLCAS 8.2* package. The simulation not only yielded the magnitude of the exchange interaction between two Gd^{III} metal ions but also reproduced the magnetic data for the Gd_2Zn and Dy_2Zn_6 complexes (Table 2). This observation supports the reliability of the calculations. The coupling constant estimated very small Ln−Ln interactions, $J_{Ln−Ln}$ = −0.0003 cm^{-1} (for the Gd_2Zn_6 complex), −0.0002 cm^{-1} (for the Dy_2Zn_6 complex), and −0.00025 (for the Tb_2Zn_6 complex), with a minor intermolecular exchange interaction of −0.001 in both. The χT versus T curves match the experimental curves, establishing the reliability of the theoretical calculations. The ground-state tunnel splitting is 0.338 cm^{-1}, which was found to occur for the Tb_2Zn_6 complex and hence support the spin relaxation through the ground state, whereas for the Dy_2Zn_6 complex for the ground state and first excited state, the tunnel splitting is less than 10^{-6} cm^{-1} and hence supports a magnetization blockade. However, these two states are very close, with a gap of ∼0.3 cm^{-1}, and the third excited state is very high in energy, rendering this molecule unsuitable for SMMs. While some of these QTMs can be quenched in the presence of an applied field, given the extremely weak exchange coupling, a significant barrier height for magnetization reversal cannot be expected.

■ CONCLUSION

The impetus for the present work was to generate luminescent−magnetic 3d−4f complexes using a newly synthesized pyridyl−pyrazolyl-based N-rich ligand. Accordingly, we have successfully synthesized four polynuclear zinc lanthanide 3d−4f complexes with {Dy_2Zn_6}, {Gd_2Zn_6}, {Tb_2Zn_6}, and {Eu_2Zn_6} cores that show an isostructural bangle-shaped topology. Interesting PL features of the Tb- and Eu-based complexes, coupled with their existence in the range of nanoscale dimension and next-to-negligible cytotoxic adverse effects, make them ideal probes for cellular investigations. Indeed, live-cell confocal microscopy images unequivocally confirm accumulation of the complexes as red and green fluorescent probes in both the nucleus and cytoplasm of the MCF7 cells. The Dy_2Zn_6 and Gd_2Zn_6 complexes, on the other hand, show some intriguing magnetic features. The magnetic measurement confirms cryogenic magnetic refrigeration of the Gd complex with an entropy change of 11.25 J kg^{-1} K^{-1} at a magnetic field of 7 T and at 2 K. Furthermore, the Dy_2Zn_6 complex shows slow magnetic relaxation associated with SMM behavior with an U_{eff} value of ∼5 K and a relaxation time of 8.52 × 10^{-6} s. One of the most fascinating aspects of this present study is the excellent synergy observed between the experimental magnetic results and the corresponding theoretical studies carried out using BS-DFT and *MOLCAS* calculations using the CASSCF method. Furthermore, theoretical results using the *ORCA* suite of programs were also found to be consistent with the absorption spectrum of the Eu_2Zn_6 and Tb_2Cl_6 complexes.

■ EXPERIMENTAL SECTION

Materials and Methods. All reagents, chemicals, and solvents that were required for this work were purchased from commercial sources and used without further purification. Elemental analysis of the compounds was done by a PerkinElmer 2400 Series-II analyzer, and the FT-IR spectra were recorded on a Nicolet MAGNA-IR-750 spectrometer with samples prepared as KBr pellets. The UV−vis spectra were collected by a PerkinElmer Lambda 950 UV−vis instrument. PL measurements of the liquid samples were performed with a Hitachi F-2500 fluorescence spectrometer. The mass spectra were recorded with the help of a Q-ToF Miro YA263 high-resolution (Waters Corp.) mass spectrometer by positive-ion-mode electrospray ionization, and the spectra were collected in a methanol medium. The powder X-ray diffraction patterns of the sample were recorded at room temperature using a Rigaku Smartlab X-ray diffractometer. The ^{1}H NMR spectra were collected on a Bruker-spectrometer operating at 400 MHz. Magnetic data of the crystalline samples were collected using a Quantum Design MPMS (Evercool, 7 T). DLS experiments were performed using a Malvern particle size analyzer (model ZEN 3690 Zetasizer Nano ZS 90, version 7.03), and TEM was performed using a Jeol JEM 2010 high-resolution transmission electron microscope.

Live-Cell Confocal Microscopy. Live-cell imaging was carried out using a confocal laser-scanning microscope (Leica TCS SP8) with a UV laser and 63X/1.4 NA oil objective equipped with a heated environmental chamber set to 37 °C with an optimal CO$_2$ facility. Briefly, MCF7 cells seeded in a covered glass-bottom dish (Genetix, Biotech Asia Pvt. Ltd.) were incubated with compounds Eu_2Zn_6 and Tb_2Zn_6 separately for 6 h. The nuclei were subsequently stained with Hoechst 33342 (Blue) (Sigma). This was followed by live-cell confocal microscopy. Images were collected and processed using the Leica software and sized in Adobe Photoshop 7.0.[76]

Cell Survival Assay. MCF7 cells (6 × 10^3) were seeded in 96-well plates (BD Biosciences, USA) and treated with the compounds Eu_2Zn_6 and Tb_2Zn_6 at the indicated concentrations. After 72 h of treatment, cell survival was assessed by 3-(4,5-dimethylthiazol-2-yl)-2,5- diphenyltetrazolium bromide (MTT) assay. Briefly, cells were washed one time with phosphate-buffered saline and treated with a MTT reagent (Sigma) for 3 h at 37 °C, and the resulting formazan was dissolved in 100 μL of DMSO. The plates were analyzed on a Molecular Devices SpectraMax M2Microplate Reader at 570 nm. The percent inhibition of viability for each concentration of the compounds was calculated with respect to the control. Data represent mean values ± standard error of mean for three independent experiments.[76]

Synthesis of H$_4$CPPC. H$_4$CPPC was synthesized with Schiff base condensation protocol. 2,6-Diacetylpyridine (1.63 g, 0.01 mol) and pyridine−pyrazole carbohydrazide[77] (4.06 g 0.02 mol) were taken in 250 mL of ethanol in a round-bottomed flask. A catalytic amount of acetic acid was mixed, and the mixture was refluxed for 24 h at 80 °C. The white precipitate thus obtained was filtered and washed with fresh ethanol several times. The product was dried at room temperature.

IR (400−4000 cm^{-1}): 3357w, 3265b, 2923w, 1691vs, 1596m, 1523vs, 1473w, 1444s, 1419vw, 1365m, 1226s, 1161m, 997m, 898s, 815w, 788m, 767w, 740w, 669w, 518w, 430w (Figure S13).

^{1}H NMR (500 MHz, [(CD$_3$)$_2$SO]): δ 14.183 (s, 2Hpyz-2H), 10.486 (s, 2H, 2NH), 8.670 (s, 2H, beside 2pyridinyl-H), 7.411 (2H meta of PyN), 7.912−8.018 (Ar−H) (Figure S14).

ESI-MS: m/z 534.2454 (M + H$^+$), 556.2286 (M + Na$^+$) (Figure S15).

Anal. Calcd (found) for C$_{27}$H$_{23}$N$_{11}$O$_2$: C, 60.78 (59.77); H, 4.35 (4.83); N, 28.88 (28.21).

Synthesis of [Eu$_2$Zn$_6$(CPPC)$_2$Cl$_{10}$(DMF)$_8$](DMF)$_2$ (Eu$_2$Zn$_6$). A 2.5 mL methanolic solution of 37.1 mg of EuCl$_3$·6H$_2$O and 13.6 mg of ZnCl$_2$ (anhydrous) was added to 53.4 mg (0.1 mmol) of H$_2$CPPC taken in 5 mL of a DMF/MeOH mixture. The resulting yellow solution was refluxed in a round-bottomed flask at 70−80 °C for 10 h. Thereafter, the solution was filtered under hot conditions into a 25 mL beaker and kept undisturbed with a paraffin cover over the mouth of the beaker. After 7 days, pillar-shaped bright-yellow crystals were obtained at the bottom of the beaker and collected by washing with a

1:1 DMF/MeOH mixture two or three times. Thus, the compound was obtained in 62% yield (based on H_4CPPC) and dried in air.

IR (KBr, cm^{-1}): 3409b, 2927vw, 1654vs, 1608w, 1550m, 1446m, 1384s, 1326w, 1303s, 1107w, 1062m, 771m, 671s, 656w (Figure S16).

Anal. Calcd (found) for $C_{90}H_{122}Cl_{10}Eu_2N_{34}O_{16}Zn_6$: C, 40.35 (40.42); H, 4.59 (4.63); N, 6.27 (6.14).

Synthesis of [Gd$_2$Zn$_6$(CPPC)$_2$Cl$_{10}$(DMF)$_8$](DMF)$_2$ (Gd$_2$Zn$_6$). The synthetic process of $[Gd_2Zn_6(CPPC)_2Cl_{10}(DMF)_8](DMF)_2$ is exactly similar to that of **Eu$_2$Zn$_6$**. In this case, GdCl$_3$·6H$_2$O was used instead of EuCl$_3$·6H$_2$O. The resultant bright-yellow solution was kept in a beaker under undisturbed conditions. Here also after 7 days, pillar-shaped bright-yellow crystals were found in 53% yield (based on H_4CPPC).

IR (KBr, cm^{-1}): 3454b, 2929vw, 1654vs, 1608w, 1550m, 1446m, 1384s, 1303s, 1108w, 1062m, 985s, 889w, 771w, 671w (Figure S17).

Anal. Calcd (found) for $C_{90}H_{122}Cl_{10}Eu_2N_{34}O_{16}Zn_6$: C, 40.35 (40.38); H, 4.59 (4.61); N, 6.27 (6.23).

Synthesis of [Tb$_2$Zn$_6$(CPPC)$_2$Cl$_{10}$(DMF)$_8$](DMF)$_2$ (Tb$_2$Zn$_6$). $[Tb_2Zn_6(CPPC)_2(Cl)_{10}(DMF)_8](DMF)_2$ was synthesized using the same procedure of **Eu$_2$Zn$_6$**, except TbCl$_3$·6H$_2$O was used in place of EuCl$_3$·6H$_2$O. After 1 week, similar kinds of crystals were obtained in 68% yield (based on H_4CPPC).

IR (KBr, cm^{-1}): 3454b, 2927vw, 1654vs, 1608w, 1562m, 1446m, 1384s, 1326w, 1303s, 1105w, 1062m, 887w, 771m, 671s (Figure S18).

Anal. Calcd (found) for $C_{90}H_{122}Cl_{10}Eu_2N_{34}O_{16}Zn_6$: C, 40.35 (40.39); H, 4.59 (4.63); N, 6.27 (6.19).

Synthesis of [Dy$_2$Zn$_6$(CPPC)$_2$Cl$_{10}$(DMF)$_8$](DMF)$_2$ (Dy$_2$Zn$_6$). A synthetic route similar to that of **Eu$_2$Zn$_6$** was followed except, instead of EuCl$_3$·6H$_2$O, 1 equiv of DyCl$_3$·6H$_2$O (36.6 mg) was added to the solution. The resultant bright-yellow solution was kept in a beaker under undisturbed conditions. After 5 days, block-shaped bright-yellow diffraction-quality crystals were obtained in 74% yield (based on H_4CPPC).

IR (KBr, cm^{-1}): 3454b, 2927vw, 1654vs, 1608w, 1558m, 1446m, 1386s, 1303s, 1108w, 1062m, 889w, 771m, 669m (Figure S19).

Anal. Calcd (found) for $C_{90}H_{122}Cl_{10}Eu_2N_{34}O_{16}Zn_6$: C, 40.35 (40.37); H, 4.59 (4.64); N, 6.27 (6.21).

Single-Crystal X-ray Diffraction. X-ray diffraction intensities for all of the complex crystals were collected at 100 K on a Bruker D8 VENTURE Microfocus diffractometer equipped with a PHOTON II detector, with Mo Kα radiation (λ = 0.710 73 Å), controlled by the *APEX3* (version 2017.3-0) software package and processed using *SAINT*. Raw data were integrated and corrected for Lorentz and polarization effects using the Bruker *APEX III* program suite. The structures were solved by direct methods in *SHELXS* and refined by full-matrix least squares on F^2 in *SHELXL*. Crystallographic data are summarized in Table S3, and CIF files for the structures reported in this paper have been deposited with the Cambridge Crystallographic Data Centre (CCDC). Deposition numbers are given in Table S3. Additional crystallographic information is available in the Table S4.

Computational Details. For estimation of the exchange coupling between Gd^{III} ions in **Gd$_2$Zn$_6$**, BS-DFT calculations have been employed on the optimized structure using the B3LYP functional[78] with the *Gaussian 09* suite[79] using the CSDZ basis set[80] for Gd, Stuttgart–Dresden ECPs (SDDs)[81,82] for La, and the TZV basis set for the rest of the atoms on the crystal structure of the **Gd$_2$Zn$_6$** complex. Noodleman's broken-symmetry approach[83] was used to extract the magnetic coupling constant between two Gd^{III} metal ions, which was further rescaled to the spins of Tb^{III} and Dy^{III} to confirm the extent of Ln–Ln exchange interaction obtained from *POLY_ANISO* simulation. There is one exchange pathway in the **Gd$_2$Zn$_6$** complex, which is the interaction between Gd1 and Gd2, termed as *J*. To evaluate the exchange coupling constant *J*, the following Hamiltonian was used.

$$\hat{H} = -2J\{(\hat{S}_{Gd1}\cdot\hat{S}_{Gd2})\}$$

For evaluation of the magnetic properties of complexes **Tb$_2$Zn$_6$** and **Dy$_2$Zn$_6$**, fragmentation of the whole complex was done in order to take one metal center at a time. We employed the basis sets [ANO-RCC···3s2p],[84] [ANO-RCC···2s], [ANO-RCC···3s2p1d], and [ANO-RCC···4s3p2d] for C, H, N, or O and Cl, respectively, and for Zn^{II} ions, we employed [ANO-RCC···5s4p2d1f], and for Ln, the basis set [ANO-RCC···8s7p5d3f2g1h] was employed, which are available in the *MOLCAS* 8.2 package.[85−87] The CASSCF method[88] was used to compute the spin free energy for the paramagnetic metal center by considering the eight and nine active electrons spanning seven 4f orbitals of Tb^{III} and Dy^{III}, respectively.

In the configuration integration procedure, the 1 octet, 48 sextets, and 392 quartets (for Gd^{III}), 7 septets, 140 quintets, and 588 triplets (for Tb^{III}), and 21 sextets (for Dy^{III}) excited states were computed for the **Gd$_2$Zn$_6$**, **Tb$_2$Zn$_6$**, and **Dy$_2$Zn$_6$** complexes respectively, to extract the anisotropy in the respective lanthanide metal centers. For the Ln metal centers, because of the hardware limitation, only a limited number of CASSCF states were mixed by spin−orbit coupling in the spin−orbit *RASSI* step.[89] To compute the local magnetic properties and **g** tensors, we employed the *SINGLE_ANISO* module,[90] in which the *ab initio*-computed matrix elements of angular momentum and spin−orbit multiplets were used. Further *POLY_ANISO* simulation of the experimental magnetic susceptibility data was done to estimate the Ln−Ln magnetic exchange coupling and plausible magnetic relaxation dynamics.

Further programs in the *ORCA* suite[91] were used for plotting of the absorption spectrum of **Eu$_2$Zn$_6$** and **Tb$_2$Zn$_6$**. For CASSCF calculations, the SARC-DKH-TZVP basis set[92,93] was used for Ln^{III} and the DKH-def2-TZVP basis set for O and Zn^{II}, whereas for the rest of atoms, the SARC-DKH-SVP basis set was used.

■ ASSOCIATED CONTENT

Ⓢ **Supporting Information**

The Supporting Information is available free of charge at https://pubs.acs.org/doi/10.1021/acs.inorgchem.1c03359.

(PDF)

Accession Codes

CCDC 2117735−2117738 contain the supplementary crystallographic data for this paper. These data can be obtained free of charge via www.ccdc.cam.ac.uk/data_request/cif, or by emailing data_request@ccdc.cam.ac.uk, or by contacting The Cambridge Crystallographic Data Centre, 12 Union Road, Cambridge CB2 1EZ, UK; fax: +44 1223 336033.

■ AUTHOR INFORMATION

Corresponding Authors

Gopalan Rajaraman − *Department of Chemistry, Indian Institute of Technology, Bombay, Powai, Mumbai 400076 Maharashtra, India;* ⬤ orcid.org/0000-0001-6133-3026; Email: rajaraman@chem.iitb.ac.in

Raju Mondal − *School of Chemical Science, Indian Association for the Cultivation of Science, Kolkata 700032 West Bengal, India;* ⬤ orcid.org/0000-0002-9013-7259; Email: icrm@iacs.res.in

Authors

Sayan Saha − *School of Chemical Science, Indian Association for the Cultivation of Science, Kolkata 700032 West Bengal, India*

Krishna Sundar Das − *School of Chemical Science, Indian Association for the Cultivation of Science, Kolkata 700032 West Bengal, India*

Tanu Sharma − *Department of Chemistry, Indian Institute of Technology, Bombay, Powai, Mumbai 400076 Maharashtra, India*

Sukhen Bala − *School of Chemical Science, Indian Association for the Cultivation of Science, Kolkata 700032 West Bengal, India*

Amit Adhikary − *School of Chemical Science, Indian Association for the Cultivation of Science, Kolkata 700032 West Bengal, India;* ⓘ orcid.org/0000-0002-1435-4585

Guo-Zhang Huang − *Key Laboratory of Bioinorganic and Synthetic Chemistry of Ministry of Education, School of Chemistry, Sun Yat-Sen University, Guangzhou 510275, P. R. China;* ⓘ orcid.org/0000-0001-9167-0090

Ming-Liang Tong − *Key Laboratory of Bioinorganic and Synthetic Chemistry of Ministry of Education, School of Chemistry, Sun Yat-Sen University, Guangzhou 510275, P. R. China;* ⓘ orcid.org/0000-0003-4725-0798

Arjit Ghosh − *School of Biological Science, Indian Association for the Cultivation of Science, Kolkata 700032 West Bengal, India*

Benubrata Das − *School of Biological Science, Indian Association for the Cultivation of Science, Kolkata 700032 West Bengal, India;* ⓘ orcid.org/0000-0003-2519-7105

Complete contact information is available at:
https://pubs.acs.org/10.1021/acs.inorgchem.1c03359

Author Contributions

†Contributed as joint first authors.

Notes

The authors declare no competing financial interest.

■ REFERENCES

(1) Chandler, M.; Minevich, B.; Roark, B.; Viard, M.; Johnson, M. B.; Rizvi, M. H.; Deaton, T. A.; Kozlov, S.; Panigaj, M.; Tracy, J. B.; Yingling, Y. G.; Gang, O.; Afonin, K. A. Controlled Organization of Inorganic Materials Using Biological Molecules for Activating Therapeutic Functionalities. *ACS Appl. Mater. Interfaces* **2021**, *13*, 39030−39041.

(2) Diab, M.; Mokari, T. Bioinspired Hierarchical Porous Structures for Engineering Advanced Functional Inorganic Materials. *Adv. Mater.* **2018**, *30*, 1706349.

(3) Ko, J.; Berger, R.; Lee, H.; Yoon, H.; Cho, J.; Char, K. Electronic effects of nano-confinement in functional organic and inorganic materials for optoelectronics. *Chem. Soc. Rev.* **2021**, *50*, 3585−3628.

(4) Li, Y.; Yu, J. Genetic engineering of inorganic functional modular materials. *Chem. Sci.* **2016**, *7*, 3472−3481.

(5) Sanchez, C.; Boissiere, C.; Cassaignon, S.; Chaneac, C.; Duruphty, O.; Faustini, M.; Grosso, D.; Laberty-Robert, C.; Nicole, L.; Portehault, D.; Ribot, F.; Rozes, L.; Sassoye, C. Molecular Engineering of Functional Inorganic and Hybrid Materials. *Chem. Mater.* **2014**, *26*, 221−238.

(6) Zang, C.; Xu, M.; Zhang, L.; Liu, S.; Xie, W. Organic−inorganic hybrid thin film light-emitting devices: interfacial engineering and device physics. *J. Mater. Chem. C* **2021**, *9*, 1484−1519.

(7) Podchezertsev, S.; Barrier, N.; Pautrat, A.; Suard, E.; Retuerto, M.; Alonso, J. A.; Fernández-Díaz, M. T.; Rodríguez-Carvajal, J. Influence of Polymorphism on the Magnetic Properties of Co$_5$TeO$_8$ Spinel. *Inorg. Chem.* **2021**, *60*, 13990−14001.

(8) Legendre, C. M.; Herbst-Irmer, R.; Stalke, D. Enhancing Steric Hindrance via Ligand Design in Dysprosium Complexes: From Induced Slow Relaxation to Zero-Field Single-Molecule Magnet Properties. *Inorg. Chem.* **2021**, *60*, 13982−13989.

(9) Rauguth, A.; Kredel, A.; Carrella, L. M.; Rentschler, E. 3d/4f Sandwich Complex Based on Metallacrowns. *Inorg. Chem.* **2021**, *60*, 14031−14037.

(10) Bera, S. P.; Mondal, A.; Konar, S. Investigation of the role of terminal ligands in magnetic relaxation in a series of dinuclear dysprosium complexes. *Inorg. Chem. Front.* **2020**, *7*, 3352−3363.

(11) Wang, H.-L.; Liu, T.; Zhu, Z.-H.; Peng, J.-M.; Zou, H.-H.; Liang, F.-P. A series of dysprosium clusters assembled by a substitution effect-driven out-to-in growth mechanism. *Inorg. Chem. Front.* **2021**, *8*, 2136−2143.

(12) Lin, P.-H.; Takase, M. K.; Agapie, T. Investigations of the Effect of the Non-Manganese Metal in Heterometallic-Oxido Cluster Models of the Oxygen Evolving Complex of Photosystem II: Lanthanides as Substitutes for Calcium. *Inorg. Chem.* **2015**, *54*, 59−64.

(13) Ferbinteanu, M.; Stroppa, A.; Scarrozza, M.; Humelnicu, I.; Maftei, D.; Frecus, B.; Cimpoesu, F. On the Density Functional Theory Treatment of Lanthanide Coordination Compounds: A Comparative Study in a Series of Cu−Ln (Ln = Gd, Tb, Lu) Binuclear Complexes. *Inorg. Chem.* **2017**, *56*, 9474−9485.

(14) Alsowayigh, M. M.; Timco, G. A.; Borilovic, I.; Alanazi, A.; Vitorica-yrezabal, I. J.; Whitehead, G. F. S.; McNaughter, P. D.; Tuna, F.; O'Brien, P.; Winpenny, R. E. P.; Lewis, D. J.; Collison, D. Heterometallic 3d−4f Complexes as Air-Stable Molecular Precursors in Low Temperature Syntheses of Stoichiometric Rare-Earth Orthoferrite Powders. *Inorg. Chem.* **2020**, *59*, 15796−15806.

(15) Boyce, S. A. J.; Moutet, J.; Niederegger, L.; Simler, T.; Nocton, G.; Hess, C. R. Influence of a Lanthanide Ion on the Ni Site of a Heterobimetallic 3d−4f Mabiq Complex. *Inorg. Chem.* **2021**, *60*, 403−411.

(16) Peng, J.-B.; Zhang, Q.-C.; Kong, X.-J.; Zheng, Y.-Z.; Ren, Y.-P.; Long, L.-S.; Huang, R.-B.; Zheng, L.-S.; Zheng, Z. High-Nuclearity 3d−4f Clusters as Enhanced Magnetic Coolers and Molecular Magnets. *J. Am. Chem. Soc.* **2012**, *134*, 3314−3317.

(17) Wu, J.; Zhao, L.; Zhang, L.; Li, X.-L.; Guo, M.; Powell, A. K.; Tang, J. Macroscopic Hexagonal Tubes of 3 d−4 f Metallocycles. *Angew. Chem., Int. Ed.* **2016**, *55*, 15574−15578.

(18) Cai, L.-Z.; Chen, Q.-S.; Zhang, C.-J.; Li, P.-X.; Wang, M.-S.; Guo, G.-C. Photochromism and Photomagnetism of a 3d−4f Hexacyanoferrate at Room Temperature. *J. Am. Chem. Soc.* **2015**, *137*, 10882−10885.

(19) Chen, W.-P.; Liao, P.-Q.; Jin, P.-B.; Zhang, L.; Ling, B.-K.; Wang, S.-C.; Chan, Y.-T.; Chen, X.-M.; Zheng, Y.-Z. The Gigantic {Ni$_{36}$Gd$_{102}$} Hexagon: A Sulfate-Templated "Star-of-David" for Photocatalytic CO$_2$ Reduction and Magnetic Cooling. *J. Am. Chem. Soc.* **2020**, *142*, 4663−4670.

(20) Li, S.-R.; Wang, H.-Y.; Su, H.-F.; Chen, H.-J.; Du, M.-H.; Long, L.-S.; Kong, X.-J.; Zheng, L.-S. A Giant 3d-4f Polyoxometalate Super-Tetrahedron with High Proton Conductivity. *Small Methods* **2021**, *5*, 2000777.

(21) Li, X.-Y.; Kang, Q.-P.; Liu, C.; Zhang, Y.; Dong, W.-K. Structurally characterized homo-trinuclear Zn (II) and hetero-pentanuclear [Zn (II)4Ln (III)] complexes constructed from an octadentatebis (Salamo)-based ligand: Hirshfeld surfaces, fluorescence and catalytic properties. *New J. Chem.* **2019**, *43*, 4605−4619.

(22) Towatari, M.; Nishi, K.; Fujinami, T.; Matsumoto, N.; Sunatsuki, Y.; Kojima, M.; Mochida, N.; Ishida, T.; Re, N.; Mrozinski, J. Syntheses, Structures, and Magnetic Properties of Acetato- and Diphenolato-Bridged 3d−4f Binuclear Complexes [M(3-MeOsaltn)(MeOH)x(ac)Ln(hfac)$_2$] (M = Zn(II), Cu(II), Ni(II), Co(II); Ln = La(III), Gd(III), Tb(III), Dy(III); 3-MeOsaltn = N,N′-Bis(3-methoxy-2-oxybenzylidene)-1,3-propanediaminato; ac = Aceta-to; hfac = Hexafluoroacetylacetonato; x = 0 or 1). *Inorg. Chem.* **2013**, *52*, 6160−6178.

(23) Yang, M.; Xie, J.; Sun, Z.; Li, L.; Sutter, J.-P. Slow Magnetic Relaxation in Ladder-Type and Single-Strand 2p–3d–4f Hetero-trispin Chains. *Inorg. Chem.* **2017**, *56*, 13482–13490.

(24) Singh, M. K.; Rajeshkumar, T.; Kumar, R.; Singh, S. K.; Rajaraman, G. Role of (1,3) {Cu-Cu} Interaction on the Magneto-Caloric Effect of Trinuclear {Cu (II)-Gd (III)-Cu (II)} Complexes: Combined DFT and Experimental Studies. *Inorg. Chem.* **2018**, *57*, 1846–1858.

(25) Feng, X.; Feng, Y.-Q.; Chen, J. J.; Ng, S.-W.; Wang, L.-Y.; Guo, J.-Z. Reticular three-dimensional 3d–4f frameworks constructed through substituted imidazole-dicarboxylate: syntheses, luminescence and magnetic properties study. *Dalton Trans.* **2015**, *44*, 804–816.

(26) Kerr, E.; Doeven, E. H.; Barbante, G. J.; Hogan, C. F.; Hayne, D. J.; Donnelly, P. S.; Francis, P. S. New perspectives on the annihilation electrogenerated chemiluminescence of mixed metal complexes in solution. *Chem. Sci.* **2016**, *7*, 5271–5279.

(27) Lu, H.; Wright, D. S.; Pike, S. D. The use of mixed-metal single source precursors for the synthesis of complex metal oxides. *Chem. Commun.* **2020**, *56*, 854–871.

(28) Andruh, M.; Costes, J.-P.; Diaz, C.; Gao, S. 3d–4f Combined Chemistry: Synthetic Strategies and Magnetic Properties. *Inorg. Chem.* **2009**, *48*, 3342–3359.

(29) Coletta, M.; McLellan, R.; Sanz, S.; Gagnon, K. J.; Teat, S. J.; Brechin, E. K.; Dalgarno, S. J. A New Family of 3d–4f Bis-Calix [4] arene-Supported Clusters. *Chem. Eur. J.* **2017**, *23*, 14073–14079.

(30) Li, X.-L.; Min, F.-Y.; Wang, C.; Lin, S.-Y.; Liu, Z.; Tang, J. Utilizing 3d–4f Magnetic Interaction to Slow the Magnetic Relaxation of Heterometallic Complexes. *Inorg. Chem.* **2015**, *54*, 4337–4344.

(31) Rosado Piquer, L.; Dey, S.; Castilla-Amorós, L.; Teat, S. J.; Cirera, J.; Rajaraman, G.; Sañudo, E. C. Microwave assisted synthesis of heterometallic 3d–4f M_4Ln complexes. *Dalton Trans.* **2019**, *48*, 12440–12450.

(32) Singh, S. K.; Beg, M. F.; Rajaraman, G. Role of Magnetic Exchange Interactions in the Magnetization Relaxation of {3d–4f} Single-Molecule Magnets: A Theoretical Perspective. *Chem. Eur. J.* **2016**, *22*, 672–680.

(33) Chorazy, S.; Zakrzewski, J. J.; Magott, M.; Korzeniak, T.; Nowicka, B.; Pinkowicz, D.; Podgajny, R.; Sieklucka, B. Octacyani-dometallates for multifunctional molecule-based materials. *Chem. Soc. Rev.* **2020**, *49*, 5945–6001.

(34) Rauguth, A.; Kredel, A.; Carrella, L. M.; Rentschler, E. 3d/4f Sandwich Complex Based on Metallacrowns. *Inorg. Chem.* **2021**, *60*, 14031–14037.

(35) Yang, X.-P.; Jones, R. A.; Wong, W.-K.; Lynch, V.; Oye, M. M.; Holmes, A. L. Design and synthesis of a near infra-red luminescent hexanuclear Zn–Nd prism. *Chem. Commun.* **2006**, 1836–1838.

(36) Peng, Y.; Singh, M. K.; Mereacre, V.; Anson, C. E.; Rajaraman, G.; Powell, A. K. Mechanism of magnetisation relaxation in {MIII2DyIII2} (M = Cr, Mn, Fe, Al) "Butterfly" complexes: how important are the transition metal ions here? *Chem. Sci.* **2019**, *10*, 5528–5538.

(37) Qiu, J.-Z.; Wang, L.-F.; Chen, Y.-C.; Zhang, Z.-M.; Li, Q.-W.; Tong, M.-L. Magnetocaloric Properties of Heterometallic 3d–Gd Complexes Based on the $[Gd(oda)_3]^{3-}$ Metalloligand. *Chem. Eur. J.* **2016**, *22*, 802–808.

(38) Li, H.; Jing, P.; Lu, J.; Xi, L.; Wang, Q.; Ding, L.; Wang, W.-M.; Song, Z. Multifunctional properties of {Cu(II)₂Ln(III)₂} systems involving nitrogen-rich nitronyl nitroxide: single-molecule magnet behaviour, luminescence, magnetocaloric effects and heat capacity. *Dalton Trans.* **2021**, *50*, 2854–2863.

(39) Maity, M.; Majee, M. C.; Kundu, S.; Samanta, S. K.; Sañudo, E. C.; Ghosh, S.; Chaudhury, M. Pentanuclear 3d–4f Heterometal Complexes of M(II)₃Ln(III)₂ (M = Ni, Cu, Zn and Ln = Nd, Gd, Tb) Combinations: Syntheses, Structures, Magnetism, and Photolumines-cence Properties. *Inorg. Chem.* **2015**, *54*, 9715–9726.

(40) Zhang, J.-W.; Kan, X.-M.; Liu, B.-Q.; Liu, G.-C.; Tian, A.-X.; Wang, X.-L. Systematic Investigation of Reaction-Time Dependence of Three Series of Copper–Lanthanide/Lanthanide Coordination

(41) Bala, S.; Bishwas, M. S.; Pramanik, B.; Khanra, S.; Fromm, K. M.; Poddar, P.; Mondal, R. Construction of Polynuclear Lanthanide {Ln = Dy (III), Tb(III), and Nd(III)} Cage Complexes Using Pyridine–Pyrazole-Based Ligands: Versatile Molecular Topologies and SMM Behaviour. *Inorg. Chem.* **2015**, *54*, 8197–8206.

(42) Chandrasekhar, V.; Hossain, S.; Das, S.; Biswas, S.; Sutter, J.-P. Rhombus-Shaped Tetranuclear $[Ln_4]$ Complexes $[Ln = Dy(III)$ and Ho(III)]: Synthesis, Structure, and SMM Behavior. *Inorg. Chem.* **2013**, *52*, 6346–6353.

(43) Ding, Y.-S.; Chilton, N. F.; Winpenny, R. E. P.; Zheng, Y.-Z. On Approaching the Limit of Molecular Magnetic Anisotropy: A Near-Perfect Pentagonal Bipyramidal Dysprosium (III) Single-Molecule Magnet. *Angew. Chem., Int. Ed.* **2016**, *55*, 16071–16074.

(44) Meseguer, C.; Titos-Padilla, S.; Hänninen, M. M.; Navarrete, R.; Mota, A. J.; Evangelisti, M.; Ruiz, J.; Colacio, E. Single-Molecule Magnet Behavior and Magnetocaloric Effect in Ferromagnetically Coupled Ln^{III}-Ni^{II}-Ni^{II}-Ln^{III} (Ln^{III} = Dy^{III} and Gd^{III}) Linear Complexes. *Inorg. Chem.* **2014**, *53*, 12092–12099.

(45) Chen, Y.-C.; Liu, J.-L.; Ungur, L.; Liu, J.; Li, Q.-W.; Wang, L.-F.; Ni, Z.-P.; Chibotaru, L. F.; Chen, X.-M.; Tong, M.-L. Symmetry-Supported Magnetic Blocking at 20 K in Pentagonal Bipyramidal Dy(III) Single-Ion Magnets. *J. Am. Chem. Soc.* **2016**, *138*, 2829–2837.

(46) Liu, J.; Chen, Y.-C.; Liu, J.-L.; Vieru, V.; Ungur, L.; Jia, J.-H.; Chibotaru, L. F.; Lan, Y.; Wernsdorfer, W.; Gao, S.; Chen, X.-M.; Tong, M.-L. A Stable Pentagonal Bipyramidal Dy(III) Single-Ion Magnet with a Record Magnetization Reversal Barrier over 1000 K. *J. Am. Chem. Soc.* **2016**, *138*, 5441–5450.

(47) Wang, H.; Qian, K.; Qi, D.; Cao, W.; Wang, K.; Gao, S.; Jiang, J. Co-crystallized fullerene and a mixed (phthalocyaninato)-(porphyrinato) dysprosium double-decker SMM. *Chem. Sci.* **2014**, *5*, 3214–3220.

(48) Yang, W.; Velkos, G.; Liu, F.; Sudarkova, S. M.; Wang, Y.; Zhuang, J.; Zhang, H.; Li, X.; Zhang, X.; Büchner, B.; Avdoshenko, S. M.; Popov, A. A.; Chen, N. Single Molecule Magnetism with Strong Magnetic Anisotropy and Enhanced Dy•••Dy Coupling in Three Isomers of Dy-Oxide Clusterfullerene $Dy_2O@C82$. *Adv. Sci.* **2019**, *6*, 1901352.

(49) ChogondahalliMuniraju, N. K.; Baral, R.; Tian, Y.; Li, R.; Poudel, N.; Gofryk, K.; Barišić, N.; Kiefer, B.; Ross, J. H.; Nair, H. S. Magnetocaloric Effect in a Frustrated Gd-Garnet with No Long-Range Magnetic Order. *Inorg. Chem.* **2020**, *59*, 15144–15153.

(50) Falsaperna, M.; Stenning, G. B. G.; da Silva, I.; Saines, P. J. Magnetocaloric $Ln(HCO_2)(C_2O_4)$ frameworks: synthesis, structure and magnetic properties. *J. Mater. Chem. C* **2021**, *9*, 13209.

(51) Jia, J.-H.; Ke, Y.-J.; Li, X.; Zhang, H.-R.; Yu, Z.-P.; Cheng, Z.-H.; Zhai, K.; Liu, Z.-Y.; Wang, J.-F. A large magnetocaloric effect of $GdCoO_3-\delta$ epitaxial thin films prepared by a polymer assisted spin-coating method. *J. Mater. Chem. C* **2019**, *7*, 14970–14976.

(52) Luo, X.-M.; Hu, Z.-B.; Lin, Q.-f.; Cheng, W.; Cao, J.-P.; Cui, C.-H.; Mei, H.; Song, Y.; Xu, Y. Exploring the Performance Improvement of Magnetocaloric Effect Based Gd-Exclusive Cluster Gd60. *J. Am. Chem. Soc.* **2018**, *140*, 11219–11222.

(53) Xu, Q.-F.; Liu, B.-L.; Ye, M.-Y.; Long, L.-S.; Zheng, L.-S. Magnetocaloric Effect and Thermal Conductivity of a 3D Coordination Polymer of $[Gd(HCOO)(C_2O_4)]_n$. *Inorg. Chem.* **2021**, *60*, 9259–9262.

(54) Han, S.-D.; Miao, X.-H.; Liu, S.-J.; Bu, X.-H. Magnetocaloric effect and slow magnetic relaxation in two dense (3,12)-connected lanthanide complexes. *Inorg. Chem. Front.* **2014**, *1*, 549–552.

(55) Li, Z.-Y.; Zhang, J.-J.; Liu, S.-Q.; Zhang, H.; Sun, Y.-J.; Liu, X.-Y.; Zhai, B. Heterometallic Hexanuclear $[Ln_4Cr_2]$ Cluster-Based Three-Dimensional Sulfate Frameworks as a Magnetic Refrigerant and Single Molecular Magnet. *Cryst. Growth Des.* **2018**, *18*, 7335–7342.

(56) Maity, S.; Mondal, A.; Konar, S.; Ghosh, A. The role of 3d–4f exchange interaction in SMM behaviour and magnetic refrigeration of carbonato bridged $Cu^{II}_2Ln^{III}_2$ (Ln = Dy, Tb and Gd) complexes of an

unsymmetrical N_2O_4 donor ligand. *Dalton Trans.* **2019**, *48*, 15170−15183.

(57) Mondal, A.; Raizada, M.; Sahu, P. K.; Konar, S. A new family of Fe_4Ln_4 (Ln = Dy^{III}, Gd^{III}, Y^{III}) wheel type complexes with ferromagnetic interaction, magnetocaloric effect and zero-field SMM behavior. *Inorg. Chem. Front.* **2021**, *8*, 4625.

(58) Cardoso Dos Santos, M.; Runser, A.; Bartenlian, H.; Nonat, A. M.; Charbonnière, L. J.; Klymchenko, A. S.; Hildebrandt, N.; Reisch, A. Lanthanide-Complex-Loaded Polymer Nanoparticles for Background-Free Single-Particle and Live-Cell Imaging. *Chem. Mater.* **2019**, *31*, 4034−4041.

(59) Hasegawa, Y.; Kitagawa, Y. Thermo-sensitive luminescence of lanthanide complexes, clusters, coordination polymers and metal−organic frameworks with organic photosensitizers. *J. Mater. Chem. C* **2019**, *7*, 7494−7511.

(60) Liu, Y.; Xie, X.-Y.; Cheng, C.; Shao, Z.-S.; Wang, H.-S. Strategies to fabricate metal−organic framework (MOF)-based luminescent sensing platforms. *J. Mater. Chem. C* **2019**, *7*, 10743−10763.

(61) Tropiano, M.; Faulkner, S. A lanthanide-based sensor for the time-gated detection of hydrogen sulfide. *Chem. Commun.* **2014**, *50*, 4696−4698.

(62) Li, L.; Zou, J.-Y.; You, S.-Y.; Cui, H.-M.; Zeng, G.-P.; Cui, J.-Z. Tuning the luminescence of two 3d−4f metal−organic frameworks for the fast response and highly selective detection of aniline. *Dalton Trans.* **2017**, *46*, 16432−16438.

(63) Xu, Q.; Chen, Z.; Min, H.; Song, F.; Wang, Y.-X.; Shi, W.; Cheng, P. Water Stable Heterometallic Zn−Tb Coordination Polymer for Rapid Detection of the Ultraviolet Filter Benzophenone. *Inorg. Chem.* **2020**, *59*, 6729−6735.

(64) Yang, X.; Hahn, B. P.; Jones, R. A.; Stevenson, K. J.; Swinnea, J. S.; Wu, Q. Reversible guest molecule encapsulation in the 3-D framework of a heteropolynuclear luminescent Zn_4Eu_2 cage complex. *Chem. Commun.* **2006**, *36*, 3827−3829.

(65) Yang, Y.; Wang, K.-Z.; Yan, D. Lanthanide doped coordination polymers with tunable afterglow based on phosphorescence energy transfer. *Chem. Commun.* **2017**, *53*, 7752−7755.

(66) Yang, Y.; Wang, K.-Z.; Yan, D. Smart Luminescent Coordination Polymers toward Multimode Logic Gates: Time-Resolved, Tribochromic and Excitation-Dependent Fluorescence/Phosphorescence Emission. *ACS Appl. Mater. Interfaces* **2017**, *9*, 17399−17407.

(67) Zhou, Z.-H.; Dong, W.-W.; Wu, Y.-P.; Zhao, J.; Li, D.-S.; Wu, T.; Bu, X.-h. Ligand-Controlled Integration of Zn and Tb by Photoactive Terpyridyl-Functionalized Tricarboxylates as Highly Selective and Sensitive Sensors for Nitrofurans. *Inorg. Chem.* **2018**, *57*, 3833−3839.

(68) Zheng, Q.; Dai, H.; Merritt, M. E.; Malloy, C.; Pan, C. Y.; Li, W.-H. A New Class of Macrocyclic Lanthanide Complexes for Cell Labelling and Magnetic Resonance Imaging Applications. *J. Am. Chem. Soc.* **2005**, *127*, 16178−16188.

(69) Meng, T.; Liu, T.; Qin, Q.-P.; Chen, Z.-L.; Zou, H.-H.; Wang, K.; Liang, F.-P. Mitochondria-localizing dicarbohydrazide Ln complexes and their mechanism of in vitro anticancer activity. *Dalton Trans.* **2020**, *49*, 4404−4415.

(70) Cirera, J.; Ruiz, E. Exchange couplingin CuIIGdIIIdinuclear complexes: A theoretical perspective. *C. R. Chim.* **2008**, *11*, 1227−1234.

(71) Liu, J. L.; Lin, W. Q.; Chen, Y. C.; Gõ mez-Coca, S.; Aravena, D.; Ruiz, E.; Leng, J. D.; Tong, M. L. CuII - GdIII cryogenic magnetic refrigerants and Cu8Dy9 singlemolecule magnet generated by in situ reactions of picolinaldehyde and acetylpyridine: Experimental and theoretical study. *Chem. Eur. J.* **2013**, *19*, 17567−17577.

(72) Milios, C. J.; Manoli, M.; Rajaraman, G.; Mishra, A.; Budd, L. E.; White, F.; Parsons, S.; Wernsdorfer, W.; Christou, G.; Brechin, E. K. A Family of [Mn6] Complexes Featuring Tripodal Ligands. *Inorg. Chem.* **2006**, *45*, 6782.

(73) Casanova, D.; Llunell, M.; Alemany, P.; Alvarez, S. The Rich Stereochemistry of Eight-Vertex Polyhedra: A Continuous Shape Measures Study. *Chem. Eur. J.* **2005**, *11*, 1479−1494.

(74) Rajeshkumar, T.; Singh, S. K.; Rajaraman, G. A computational perspective on magnetic coupling, magneto-structural correlations and magneto-caloric effect of a ferromagnetically coupled {GdIII−GdIII} Pair. *Polyhedron* **2013**, *52*, 1299−1305.

(75) Bala, S.; Huang, G.-Z.; Ruan, Z.-Y.; Wu, S.-G.; Liu, Y.; Wang, L.-F.; Liu, J.-L.; Tong, M.-L. A square antiprism dysprosium single-ion magnet with an energy barrier over 900 K. *Chem. Commun.* **2019**, *55*, 9939−9942.

(76) Ghosh, A.; Bhattacharjee, S.; Chowdhuri, S. P.; Mallick, A.; Rehman, I.; Basu, S.; Das, B. B. SCAN1-TDP1 trapping on mitochondrial DNA promotes mitochondrial dysfunction and mitophagy. *Sci. Adv.* **2019**, *5*, 9778.

(77) Saha, S.; De, A.; Ghosh, A.; Ghosh, A.; Bera, K.; Das, K. S.; Akhtar, S.; Maiti, N. C.; Das, A. K.; Das, B. B.; Mondal, R. Pyridine-pyrazole based Al(iii) 'turn on' sensor for MCF7 cancer cell imaging and detection of picric acid. *RSC Adv.* **2021**, *11*, 10094−10109.

(78) Lee, C.; Yang, W.; Parr, R. G. Development of the Colle-Salvetti correlation-energy formula into a functional of the electron density. *Phys. Rev. B* **1988**, *37*, 785−789.

(79) Frisch, M.; Trucks, G.; Schlegel, H. B.; Scuseria, G.; Robb, M.; Cheeseman, J.; Scalmani, G.; Barone, V.; Mennucci, B.; Petersson, G.; et al. *Gaussian 09*, revision A.02; Gaussian. Inc.: Wallingford, CT, 2009; Vol. *200*, p 28.

(80) Cundari, T. R.; Stevens, W. J. Effective core potential methods for the lanthanides. *J. Chem. Phys.* **1993**, *98*, 5555−5565.

(81) Andrae, D.; Häußermann, U.; Dolg, M.; Stoll, H.; Preuß, H. Energy-adjustedab initio pseudopotentials for the second and third row transition elements. *Theor. Chim. Acta* **1990**, *77*, 123−141.

(82) Dolg, M.; Wedig, U.; Stoll, H.; Preuss, H. Energy-adjusted ab initio pseudopotentials for the first-row transition elements. *J. Chem. Phys.* **1987**, *86*, 866−872.

(83) Noodleman, L. Valence bond description of antiferromagnetic coupling in transition metal dimers. *J. Chem. Phys.* **1981**, *74*, 5737−5743.

(84) Roos, B. r. O.; Lindh, R.; Malmqvist, P.-Å.; Veryazov, V.; Widmark, P.-O.; Borin, A. C. New relativistic atomic natural orbital basis sets for lanthanide atoms with applications to the Ce diatom and LuF_3. *J. Phys. Chem. A* **2008**, *112*, 11431−11435.

(85) Karlström, G.; Lindh, R.; Malmqvist, P.-Å.; Roos, B. O.; Ryde, U.; Veryazov, V.; Widmark, P.-O.; Cossi, M.; Schimmelpfennig, B.; Neogrady, P.; Seijo, L. MOLCAS: a program package for computational chemistry. *Comput. Mater. Sci.* **2003**, *28*, 222−239.

(86) Veryazov, V.; Widmark, P. O.; Serrano-Andrés, L.; Lindh, R.; Roos, B. O. 2MOLCAS as a development platform for quantum chemistry software. *Int. J. Quantum Chem.* **2004**, *100*, 626−635.

(87) Aquilante, F.; De Vico, L.; Ferré, N.; Ghigo, G.; Malmqvist, P. å.; Neogrády, P.; Pedersen, T. B.; Pitoňák, M.; Reiher, M.; Roos, B. O.; et al. MOLCAS 7: the next generation. *J. Comput. Chem.* **2010**, *31*, 224−247.

(88) Malmqvist, P. Å.; Roos, B. O.; Schimmelpfennig, B. The restricted active space (RAS) state interaction approach with spin−orbit coupling. *Chem. Phys. Lett.* **2002**, *357*, 230−240.

(89) Malmqvist, P. Å.; Roos, B. O.; Schimmelpfennig, B. The restricted active space (RAS) state interaction approach with spin−orbit coupling. *Chem. Phys. Lett.* **2002**, *357*, 230−240.

(90) Chibotaru, L. F.; Ungur, L. Ab initio calculation of anisotropic magnetic properties of complexes. I. Unique definition of pseudospin Hamiltonians and their derivation. *J. Chem. Phys.* **2012**, *137*, 064112.

(91) Neese, F. The ORCA program system. *Wires Comput. Mol. Sci.* **2012**, *2*, 73−78.

(92) Wolf, A.; Reiher, M.; Hess, B. A. The generalized Douglas−Kroll transformation. *J. Chem. Phys.* **2002**, *117*, 9215−9226.

(93) Pantazis, D. A.; Neese, F. All-Electron Scalar Relativistic Basis Sets for the Lanthanides. *J. Chem. Theory Comput.* **2009**, *5*, 2229−2238.